Research Article | Vol. 9, No. 11 | 1 Nov 2018 | BIOMEDICAL OPTICS EXPRESS 5809

Biomedical Optics EXPRESS

Fast-scanning photoacoustic microscopy with a side-looking fiber optic ultrasound sensor

YIZHI LIANG,[1,2] JIN-WEI LIU,[1] LONG JIN,[1,4] BAI-OU GUAN,[1] AND LIDAI WANG[2,3,5]

[1]*Guangdong Provincial Key Laboratory of Optical Fiber Sensing and Communications, Institute of Photonics Technology, Jinan University, Guangzhou 510632, China*
[2]*Department of Mechanical and Biomedical Engineering, City University of Hong Kong, 83 Tat Chee Ave, Kowloon, Hong Kong SAR, China*
[3]*City University of Hong Kong Shenzhen Research Institute, Yuexing Yi Dao, Nanshan District, Shenzhen, Guang Dong, 518057, China*
[4]*iptjinlong@gmail.com*
[5]*lidawang@cityu.edu.hk*

Abstract: Optical-resolution photoacoustic microscopy (OR-PAM) images biological tissue with sub-cellular resolution and optical absorption contrast. OR-PAM is limited by the tradeoff among imaging speed, field of view, and sensitivity. In this work, we present an OR-PAM technique based on an unfocused side-looking fiber optic ultrasound (FOUS) sensor, which achieves high imaging speed, large field of view, and good sensitivity for *in vivo* imaging. The FOUS sensor is developed based on a dual-polarized fiber laser and read out with real-time frequency demodulation. Via minimizing the readout noise, the sensor offers a noise-equivalent pressure of 43.6 Pa, enabling high detection sensitivity over a large field of view. High imaging speed is achieved via scanning the laser beam with a 2D galvo mirror in the ultrasound detection area. Microvascular imaging with a frame rate of 2 Hz over a 2 × 2 mm^2 area has been demonstrated in the mouse ear. The new OR-PAM technique may be used in the visualization of biological and physiologic dynamics.

© 2018 Optical Society of America under the terms of the OSA Open Access Publishing Agreement

1. Introduction

Optical-resolution photoacoustic microscopy (OR-PAM) images optical absorption contrast at sub-cellular spatial resolution [1–7]. In OR-PAM, a focused laser beam induces initial pressure rise along the optical axis. An ultrasound transducer detects the pressure wave, generating a depth-resolved 1D image (an A-line). To achieve high sensitivity, the focused ultrasound beam is confocally aligned with the optical excitation beam. A 3D image is obtained by raster scanning the optical and ultrasound beams together. Translating the OR-PAM probe with a precision stage may be slow mainly due to the mass of the probe. It usually takes several to tens of minutes to acquire a high-resolution image over a large field of view [8,9]. Capturing dynamic processes, such as neurovascular coupling and circulating tumor cells, need a fast imaging speed. Using a voice-coil [10] or water-immersible mirror scanner [11–15], the imaging speed has been increased by tens to hundreds of folds, enabling many fast imaging applications. For the water-immersible mirror scanner systems, the presence of the water is the major limit of the scanning speed. Another fast imaging approach is to scan the optical beam only and keep the acoustic beam stationary [16,17]. In such a configuration, the field of view is limited by the acoustic detection area. An ultrasound sensor with both large detection area and high sensitivity is needed in the optical scanning approach. For instance, a polymer micro-ring resonator was used to perform single-cell imaging with superior spatial resolution [18]. Several fiber optic ultrasound sensors, e.g., on-tip Fary-Perot or π-shift Bragg grating ultrasound sensors, have been developed for OR-PAM [19,20]. The fiber sensor has miniature size, large detection area, and excellent sensitivity. The passive

#336107 https://doi.org/10.1364/BOE.9.005809
Journal © 2018 Received 27 Jun 2018; revised 9 Oct 2018; accepted 16 Oct 2018; published 29 Oct 2018

optical resonator needs to work within a narrow spectral range to gain a good sensitivity. A tunable laser is needed to detect acoustically induced resonance shift. In contrast, a fiber laser is exploited as ultrasound sensor, which intrinsically offers narrow linewidth and high sensitivity.

Previously, we reported a similar laser-based fiber optic ultrasound sensor (FOUS) and demonstrated its application in OR-PAM [21]. However, the signal-to-noise ratio (SNR) was insufficient for imaging biological tissue, and the imaging speed was limited by a slow frequency demodulation system. To address these problems, a photodetector with high optical power handling (Discovery, DSC40S) is used to improve the SNR. Furthermore, using the vector signal analyzer (NI Pxie-5646R) as a fast demodulation system, we achieved real-time data acquisition, processing and image display, which allows for fast *in vivo* imaging. The sensor offers mm-sized field of view, which avoids acoustic-beam scanning. Using the FOUS sensor and a dual-axis galvo mirror scanner, we develop a fast-scanning wide-field OR-PAM system with a high SNR. *In vivo* imaging of microvasculature is demonstrated with a field of view of 2 × 2 mm^2 at 2 Hz.

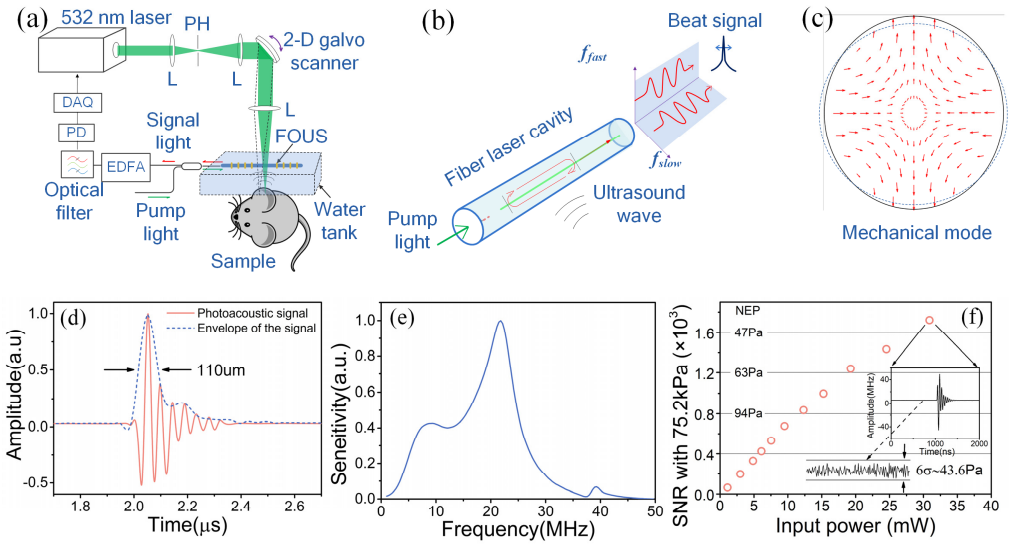

Fig. 1. (a) Schematic of OR-PAM system. (b) Principle of the FOUS sensor. (c) Calculated fiber deformation under 22-MHz ultrasound excitation. (d) Demodulated photoacoustic signal in time domain. (e) Amplitude spectrum of the demodulated signal in (d). (f) Measured SNR and noise-equivalent pressure (NEP) as a function of input power at the photodetector. The noise floor is characterized as six times of the noise standard deviation. In the SNR measurement, the incident acoustic pressure is 75.2 kPa.

2. Ultrasound detection

Figure. 1(a) shows the schematic of the OR-PAM system incorporating the side-looking FOUS sensor. A 532-nm pulsed laser (VPFL-G-20, Spectral Physics) is employed as the excitation light source. The pulse width is 3 ns. The 1.2 mm laser beam is expanded by two lenses to about 6 mm in diameter. And reflected on a two-axis galvo scanner. Then the laser beam is focused into the sample with an objective lens (AC127-025-A, Thorlabs, NA = 0.1 in air). An optical window is placed between the air and water to maintain a stable optical interface. The water-immersed FOUS sensor is mounted horizontally at a position of 1.6 mm above the sample surface. Volumetric images are acquired via scanning the optical beam along the x and y-axes. An FPGA card (PCIe-7852R, National Instruments) synchronizes the laser excitation, galvo scanning and data acquisition.

Biomedical Optics EXPRESS

Figure. 1(b) shows the principle of ultrasound detection using the FOUS sensor [21]. The sensor is based on a dual-polarized fiber laser. Two Bragg grating reflectors in an Er/Yd co-doped fiber forms a Fabry-Perot cavity. Each grating is 3 mm in length, and the two are separated by 2 mm. The fiber laser emits two orthogonal polarization modes at ~1530 nm. Because of weak birefringence of the optical fiber, the two polarization modes have a small difference in the lasing frequency, which generates a radio-frequency beat signal (carrier frequency f_c = ~2.2 GHz) on a photodiode detector. A 45-degree oriented polarizer is placed before the photodetector to enhance the beat signal. Ultrasound pressure along the fiber radius may modulate the beat frequency. The acoustically modulated beat signal can be measured using I/Q demodulation. The beat signal is mixed with two quadrature radio frequency signals, which have the same frequency and 90-degree phase offset. After the mixing, two baseband signals I and Q are used to recover the modulated signal. The phase information can be extracted via $\phi = \arctan(Q/I)$. The frequency variation of the beat signal can be recovered by taking the derivative of the phase. The beat signal is processed in a vector signal analyzer (NI Pxie-5646R). By down-converting the beat signal, the data sampling rate is reduced to 100MHz, which enables real-time data acquisition.

A photoacoustic signal from a point source is recorded as shown in Fig. 1(d). Figure 1(e) shows the spectrum of the same photoacoustic signal. Ultrasound wave may also excite axial symmetrical modes (zeroth-order azimuthal modes), which is similar with PZT transducer. Because these modes induce the same frequency shift on all radial directions, the FOUS sensor detects the frequency difference between two polarizations and thus does not respond to the common-mode excitation. Figure 1(c) shows the first-order radial/second-order azimuthal mode. This mode dominants in the frequency range of interest (tens of MHz). The central frequency of this mechanic mode is ~22 MHz and the −6 dB bandwidth is ~70%. This provides 110µm axial resolution as shown in Fig. 1(d) and (e), which is slightly worse than conventional ultrasound transducer due to limited bandwidth. The center frequency depends on the diameter of the sensor (~125µm) and can be increased via etching the fiber with hydrofluoric acid. In [21], a 65-µm sensor provides 40MHz center frequency and almost doubles the axial resolution. Figure 1(f) exhibits the measured SNR at different fiber-laser powers. An unfocused ultrasound transducer (V214-BC-RM, Panametrics) emitted an ultrasound wave with a frequency range from 5 to 31 MHz. A hydrophone (HMB-0500, ONDA) measures the peak-to-peak acoustic pressure as 75.2 kPa. The front surface of the unfocused ultrasound transducer was placed in parallel with the fiber optic sensor. The noise floor is estimated from six times of the noise standard deviation. The SNR is mainly limited by the noise figure of the photodetector. In high input power regime, the dominant noise source is shot noise, and the SNR is approximately proportional to the square root of the optical power [23] [24]. To have a high signal to noise ratio, we want to increase the incident optical power as high as possible, and have the photodetector work in the shot noise limited region. Eventually, saturation of the photodetector will limit optical power. Therefore, we use a high-power photodetector (Discovery, DSC40S), as well as increasing the fiber laser power, to improve the SNR. As a result, the shot noise is decreased by ~3 dB compared with our previous result [21]. When the input power on the photodiode is 30 mW, the noise-equivalent pressure (NEP) is ~43.6 Pa with a 50-MHz acquisition bandwidth. To achieve fast *in vivo* imaging, we implemented real-time data acquisition, processing and image display.

We experimentally compare the sensitivity and linearity between the present FOUS sensor and a commercial ultrasound transducer (V214-BC-RM, Olympus). The center frequency of the this transducer are 50MHz and have 80% −6dB bandwidth. Figure 2(a) shows the experimental setup. A black tape is used as an optical absorber to generate photoacoustic signal. The commercial transducer is 6-mm in diameter and is placed under the tape. The output signal is first amplified by 39 dB with an ultrasonic pulse receiver (5073 PR, Olympus), then filtered with a 50-MHz low-pass filter (BLP50 + , Mini Circuits), and eventually digitized and recorded in computer. The FOUS sensor is placed above the black

Biomedical Optics EXPRESS

tape. The two sensors are 1.5 mm away from the black tape, so that the received ultrasound pressures are almost the same in amplitude. Figure 2(b) shows two measured photoacoustic signals. The FOUS sensor has a 16.3-dB higher SNR than the commercial ultrasound transducer. To validate the linearity of the FOUS sensor, we measure different photoacoustic pressures using both the FOUS sensor and the commercial transducer. Figure 2(c) shows the comparison between the measurements from the two sensors. The FOUS measurement is highly linear with the measurement of the commercial transducer, the coefficient of determination is 0.99.

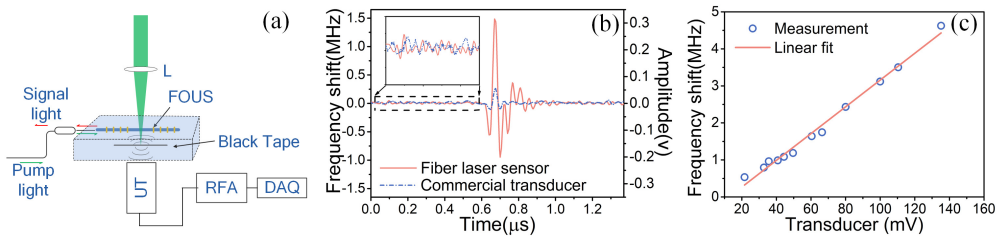

Fig. 2. Comparison between the present FOUS and an unfocused piezoelectric ultrasound transducer. (a) Experimental setup. L: lens, RFA: radio-frequency amplifier. UT: ultrasound transducer. DAQ: data acquisition.(b) Recorded temporal photoacoustic signals. (c) Peak-to-peak amplitudes at different signal strengths.

3. OR-PAM

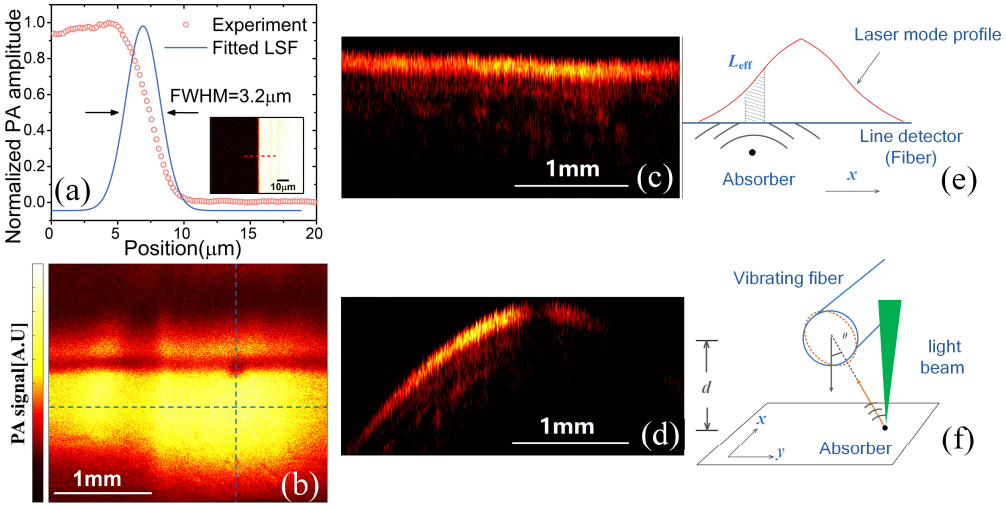

Fig. 3. (a) Lateral resolution test result. The line spread function (LSF) is calculated from the photoacoustic amplitude profile normal to a sharp blade edge. (b) Maximum amplitude projection (MAP) image of the black tape. Scale bar: 1 mm. (c, d) B-scan images of black tape along the horizontal and vertical dashed lines in (b). Scale bar: 1 mm. (e) Schematic showing that the FOUS sensor works as a line detector along the fiber length. (f) In the radial direction, the sensitivity of the FOUS sensor depends on the acoustic incident angle θ.

To characterize the lateral resolution, we imaged a sharp blade edge. The scanning step size is 0.18 μm. Figure 3(a) shows the maximum amplitude profile along the dashed line in the insert. The amplitude profile was averaged 20 times to yield a smooth edge spread function (ESF). By fitting the ESF with an error function, we calculated the line spread function and estimated the lateral resolution as 3.2 μm, which is close to the diffraction limited optical focal spot size (2.71μm for NA = 0.1, wavelength 532nm). The degraded resolution may be caused by aberration of the imaging system.

Biomedical Optics EXPRESS

To measure the field of view (FOV), we raster scanned the laser beam over a black tape, assuming that the sample has spatially uniform absorption. The FOUS sensor was 1.6-mm above the sample. Figure 3(b) shows a maximum amplitude projection (MAP) image over 3 × 3 mm^2. The −6dB FOV is ~3 × 1.6mm^2. The FOUS sensor partially blocks the optical beam and casts a shadow in the MAP image. Figure 3(c) and (d) exhibit two cross-sectional images along the two dashed lines marked in Fig. 3(b). Along the fiber, the FOUS sensor works as a line detector. As shown in Fig. 3(e), a spherical ultrasound wave can effectively excite only a small region, whose dimension is comparable to the acoustic wavelength and is much shorter than the laser cavity [22]. As a result, the sensitivity along the fiber is proportional to the profile of the intracavity intensity, which is determined by the gain medium, the grating coupling efficiency, and the cavity length. Along the radial direction of the fiber, the FOUS can be treated as a point detector, as shown in Fig. 3(f). The sensitivity on the radial direction depends on the angle θ between the ultrasound incidence direction and the fiber principle axis, following a |cos(2θ)| function. The view angle is ~60 degrees. The variation in depth in Fig. 3(d) is due to the distance change between the sensor and the acoustic source when scanning across the fiber sensor.

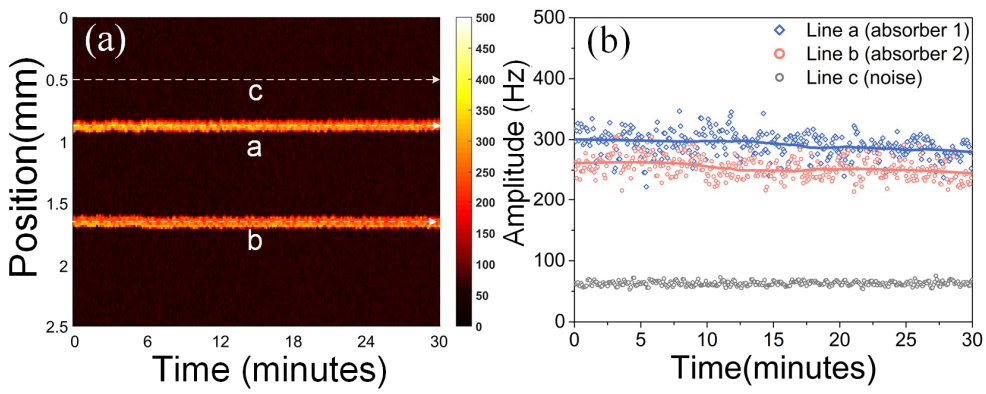

Fig. 4. (a) B-Scan MAP image of two hair as absorb for 30 minutes (b) Date extracted from 3 dash line of the Fig. 4(a).

Here we perform continuous imaging to test the stability of the sensor in this OR-PAM system. We image two human hairs in B-scan mode. The B-Scan rate is 0.2Hz, and we acquire data for 30 minutes. The images are shown in Fig. 4(a) and (b). No noticeable variation of the sensitive was observed. We also observed that, even with vibration or temperature change, the FOUS sensor remains stable with high sensitivity [21]. In a previous report [21], we scan the sensor at ~10 mm/s in water and find the FOUS remains stable due to the heterodyning detection.

The imaging speed was tested by imaging black ink flowing in a transparent plastic tube. Each frame covers an area of 2.8 × 1 mm^2 with 200 × 100 pixels. The repetition rate of the pulsed laser is 160 kHz. The scanning speed along the fast and slow axes are 400 and 2 Hz, respectively. The 3D imaging rate is 4 Hz. Figure 5(a) shows four consecutive snapshots captured by the OR-PAM system. The average flow speed was calculated as 1.4 mm/s, in good agreement with the set value.

We imaged the mouse ear to demonstrate *in vivo* imaging. All procedures involving animals were approved by the animal ethical committee of City University of Hong Kong. The laser pulse repetition rate is 100 kHz. The scanning rates along the fast and slow axes are 100 and 0.2 Hz, respectively. One image has 500 × 500 pixels over a scanning area of 2.2 × 2.2 mm^2. The laser pulse energy on the tissue surface is 300 nJ. The lateral resolution is 3.2 μm. For our imaging system, due to the beam divergence, the surface fluence about 60

Biomedical Optics EXPRESS

mJ/cm^2 when focusing at 118 µm deep. Please note that the surface fluence might be different when focusing at different depths. This fluence is still above the ANSI safety limit. In the future, we will make further effort to improve the SNR and lower the fluence for *in vivo* imaging. Figure 5(c) shows an MAP (maximum amplitude projection) image of microvessels in the mouse ear. Both trunk vessels and capillaries can be resolved in the image. A volumetric image of the mouse ear is shown in Fig. 5(d) and Visualization 2.

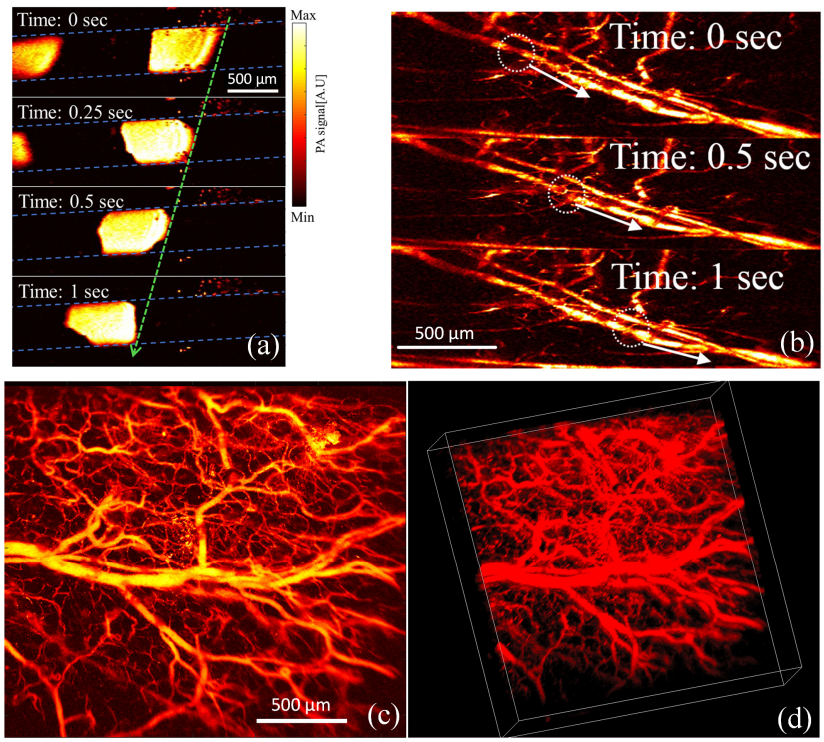

Fig. 5. (a) OR-PAM of black ink flowing in a plastic tube at 4 Hz. The blue dashed lines show the boundaries of the tube. scale bar: 500 µm (b) Fast imaging of blood flow in the mouse ear (see Visualization 1). Pixel number 200 × 200, scanning area 2 × 2 mm^2, frame rate 2 Hz. Scale bar: 500 µm. Three consecutive snapshots in the dashed white circle shows the blood flow. (c) *In vivo* imaging of the mouse ear. Pixels 500 × 500, scanning area 2.2 × 2.2 mm^2, frame rate 0.2 Hz. Scale bar 500 µm. (d) three-dimensional volumetric images for the *in vivo* imaging of mouse ear, the dimension of the white box is 2.2 × 2.2 × 0.52mm (Visualization 2).

To image hemodynamics, the scanning rate was increased to 2 Hz with a FOV of 2 × 2 mm^2. The laser repetition rate was 160 kHz. The B-scan rate was 400 Hz. Each volumetric image has 200 × 200 A-lines. The step size in the lateral direction is 10 µm. This imaging speed enables recording blood flow in both trunk vessels and capillaries. The highest measurable flow speed is 4mm/s in the transverse plane. Figure 5(b) shows three consecutive snapshots with a time interval of 0.5 seconds. More results are shown in the Visualization 1, the negative contrast feature was enhance by 40% in the video. We can see a negative contrast feature flowing in the blood vessel. The flow speed in an 82-µm-diameter vessel is calculated as 0.57mm/s. In a 34-µm-diameter vessel, the flow speed is 0.32 mm/s.

4. Conclusion

In summary, we present a fast-scanning OR-PAM technique based on a fiber optic ultrasound sensor. The ultrasound sensor is side looking and unfocused, providing a large field-of-view. Moreover, the ultrasound sensor has narrow linewidth and a differential detection mechanism,

Biomedical Optics EXPRESS

offering both high sensitivity and great stability. In OR-PAM, the ultrasound sensor remains stationary, and the excitation laser beam is rapidly scanned in the air. By optimizing the detection sensitivity and increasing the real-time imaging speed, we develop OR-PAM with large field of view, high speed, and good sensitivity. We have demonstrated *in vivo* OR-PAM with a 2 × 2 mm^2 FOV at a volumetric rate of 2 Hz. The fast scanning speed enables imaging physiologic dynamics in both trunk vessels and capillaries.

Funding

Research Grants Council of the Hong Kong Special Administrative Region (21205016, 11215817); City University of Hong Kong startup grant (7200474, 9610339); Shenzhen Basic Research Project (JCYJ20160329150236426, JCYJ20170413140519030); National Natural Science Foundation of China (NSFC) (61775083, 81627805, 61805102); Natural Science Foundation of Guangdong Province (S2013030013302).

Disclosures

The authors declare that there are no conflicts of interest related to this article.

References

1. L. V. Wang and J. Yao, "A practical guide to photoacoustic tomography in the life sciences," Nat. Methods **13**(8), 627–638 (2016).
2. P. Hai, J. Yao, K. I. Maslov, Y. Zhou, and L. V. Wang, "Near-infrared optical-resolution photoacoustic microscopy," Opt. Lett. **39**(17), 5192–5195 (2014).
3. O. Simandoux, N. Stasio, J. Gateau, J. P. Huignard, C. Moser, D. Psaltis, and E. Bossy, "Optical-resolution photoacoustic imaging through thick tissue with a thin capillary as a dual optical-in acoustic-out waveguide," Appl. Phys. Lett. **106**(9), 094102 (2015).
4. P. K. Upputuri and M. Pramanik, "Fast photoacoustic imaging systems using pulsed laser diodes: a review," Biomed. Eng. Lett. **8**(2), 1–15 (2018).
5. X. Shu, H. Li, B. Dong, C. Sun, and H. F. Zhang, "Quantifying melanin concentration in retinal pigment epithelium using broadband photoacoustic microscopy," Biomed. Opt. Express **8**(6), 2851–2865 (2017).
6. W. Liu and H. F. Zhang, "Photoacoustic imaging of the eye: A mini review," Photoacoustics **4**(3), 112–123 (2016).
7. R. Cao, J. Li, B. Ning, N. Sun, T. Wang, Z. Zuo, and S. Hu, "Functional and oxygen-metabolic photoacoustic microscopy of the awake mouse brain," Neuroimage **150**, 77–87 (2017).
8. K. Maslov, H. F. Zhang, S. Hu, and L. V. Wang, "Optical-resolution photoacoustic microscopy for *in vivo* imaging of single capillaries," Opt. Lett. **33**(9), 929–931 (2008).
9. S. Hu, K. Maslov, and L. V. Wang, "Second-generation optical-resolution photoacoustic microscopy with improved sensitivity and speed," Opt. Lett. **36**(7), 1134–1136 (2011).
10. L. Wang, K. Maslov, J. Yao, B. Rao, and L. V. Wang, "Fast voice-coil scanning optical-resolution photoacoustic microscopy," Opt. Lett. **36**(2), 139–141 (2011).
11. J. Yao, L. Wang, J.-M. Yang, K. I. Maslov, T. T. W. Wong, L. Li, C.-H. Huang, J. Zou, and L. V. Wang, "High-speed label-free functional photoacoustic microscopy of mouse brain in action," Nat. Methods **12**(5), 407–410 (2015).
12. J. Y. Kim, C. Lee, K. Park, G. Lim, and C. Kim, "Fast optical-resolution photoacoustic microscopy using a 2-axis water-proofing MEMS scanner," Sci. Rep. **5**(1), 7932 (2015).
13. K. Park, J. Y. Kim, C. Lee, S. Jeon, G. Lim, and C. Kim, "Handheld photoacoustic microscopy probe," Sci. Rep. **7**(1), 13359 (2017).
14. J. Y. Kim, C. Lee, K. Park, S. Han, and C. Kim, "High-speed and high-SNR photoacoustic microscopy based on a galvanometer mirror in non-conducting liquid," Sci. Rep. **6**(1), 34803 (2016).
15. L. Lin, J. Yao, R. Zhang, C. C. Chen, C. H. Huang, Y. Li, L. Wang, W. Chapman, J. Zou, and L. V. Wang, "High-speed photoacoustic microscopy of mouse cortical microhemodynamics," J. Biophotonics **10**(6-7), 792–798 (2017).
16. L. Li, C. Yeh, S. Hu, L. Wang, B. T. Soetikno, R. Chen, Q. Zhou, K. K. Shung, K. I. Maslov, and L. V. Wang, "Fully motorized optical-resolution photoacoustic microscopy," Opt. Lett. **39**(7), 2117–2120 (2014).
17. Z. Xie, S. Jiao, H. F. Zhang, and C. A. Puliafito, "Laser-scanning optical-resolution photoacoustic microscopy," Opt. Lett. **34**(12), 1771–1773 (2009).
18. B. Dong, H. Li, Z. Zhang, K. Zhang, S. Chen, C. Sun, and H. F. Zhang, "Isometric multimodal photoacoustic microscopy based on optically transparent micro-ring ultrasonic detection," Optica **2**(2), 169–176 (2015).
19. R. Shnaiderman, G. Wissmeyer, M. Seeger, D. Soliman, H. Estrada, D. Razansky, A. Rosenthal, and V. Ntziachristos, "Fiber interferometer for hybrid optical and optoacoustic intravital microscopy," Optica **4**(10), 1180–1186 (2017).

Biomedical Optics EXPRESS

20. T. J. Allen, O. Ogunlade, E. Zhang, and P. C. Beard, "Large area laser scanning optical resolution photoacoustic microscopy using a fibre optic sensor," Biomed. Opt. Express **9**(2), 650–660 (2018).
21. Y. Liang, L. Jin, L. Wang, X. Bai, L. Cheng, and B. O. Guan, "Fiber-laser-based ultrasound sensor for photoacoustic imaging," Sci. Rep. **7**(1), 40849 (2017).
22. X. Bai, Y. Liang, H. Sun, L. Jin, J. Ma, B. O. Guan, and L. Wang, "Sensitivity characteristics of broadband fiber-laser-based ultrasound sensors for photoacoustic microscopy," Opt. Express **25**(15), 17616–17626 (2017).
23. H. Jiang, J. Taylor, F. Quinlan, T. Fortier, and S. A. Diddams, "Noise Floor Reduction of an Er:Fiber Laser-Based Photonic Microwave Generator," IEEE Photonics J. **3**(6), 1004–1012 (2011).
24. J. Taylor, S. Diddams, S. Datta, and A. Joshi, "Photodiode limitations in the generation of low-noise microwave signals from stable frequency combs," International Topical Meeting on Microwave Photonics, 1–3 (2009).